Revision 1

Si-magnetite Nano-precipitates in Silician Magnetite from Banded Iron Formation: Z-contrast Imaging and *ab initio* Study

Huifang Xu*, Zhizhang Shen, and Hiromi Konishi

NASA Astrobiology Institute, Department of Geoscience and Material Science Program
University of Wisconsin-Madison
1215 W Dayton St., Madison, WI 53706, USA

Madison, Wisconsin 53706

Running title: Si-magnetite nano-precipitates in magnetite

* Corresponding author: Dr. Huifang Xu

Tel: 1-608-265-5887

Fax: 1-608-262-0693

Email: hfxu@geology.wisc.edu

Abstract

Si-bearing magnetite or silician magnetite is common in low and high temperature rocks. However, details about possible Fe-silicate or Si-Fe-oxide discrete phases / nano-precipitates were not available due to the limitations of conventional high-resolution TEM. Combining Z-contrast imaging and *ab initio* calculation using density functional theory (DFT) method, we have derived both composition and crystals structure of the discrete nano-precipitates within host magnetite. The nano-precipitates of Si-magnetite with composition of $[\square_{0.5}$ $Fe^{2+}{}_{0.5}]^{VI}[Fe^{3+}]^{VI}Si^{IV}O_4$ or γ-$Fe_{1.5}SiO_4$ occur in silician magnetite from a banded iron formation from Western Australia. In the Si-magnetite precipitates, Si replaces Fe^{3+} in tetrahedral sites of the magnetite structure and vacancies are introduced in the octahedral Fe^{2+} sites. The Si-magnetite precipitates distribute along {111} of the host magnetite. Widths of the precipitates are even multiples of d_{111} of magnetite, such as $2d_{111}$, $4d_{111}$, and $6d_{111}$. Ordering of the vacancies in the Si-magnetite will result in symmetry of $P4_332$, which is a subgroup of $Fd3m$ for magnetite. Stacking of Si-magnetite and magnetite (111) layers along the [111] direction also occur in magnetite. The nano-precipitates result from exsolution of Si-magnetite from the host silician magnetite at low-temperature. The occurrence of the thin nano-precipitates within the magnetite host results from the minimization of interfacial energy between the precipitate and the host magnetite. Relatively high concentration of aqueous silica and Fe-silicate complex species in pore fluid might enhance the incorporation of Si into the silician magnetite during crystallization of the magnetite.

Keywords: Si-magnetite, silician magnetite, banded iron formation, Z-contrast imaging, DFT

Introduction

There are more than 30 reported studies documenting the presence of silician magnetite included in a wide range of rock types from low to high temperatures. These rock types include banded iron formations, mid-ocean ridge serpentinites, volcanogenic massive sulfide (VMS) deposits, skarns and porphyries, as well as high temperature igneous occurrences ranging from felsic to gabbroic compositions, pegmatites, and carbonatites (see a summary by Huberty et al., 2012). Early studies report a range in SiO_2 of up to 8 wt% for silician magnetite, especially the magnetite from Porphyry and Skarn ore deposits (Shimazaki, 1998; Shiga, 1988, 1989; Westendorp et al. 1991; Takagi, 1992; Wang et al., 2001; Imai 2001; Ohwaka et al., 2007; Huberty et al., 2012).

Results from in-situ X-ray micro-diffraction and TEM observations indicate that Si atoms occupy magnetite lattice sites, instead of existing as silica inclusions (Newberry et al., 1982; Huberty et al., 2012). Guinier-Preston (G.P.) zone-like textures have been observed in a few instances suggesting the presence of nano-scale γ-Fe_2SiO_4 domains (Huberty et al., 2012). However, further details related to possible Fe-silicate discrete phases / nano-precipitates were not available due to the limitations of conventional high-resolution TEM (HRTEM), which is a phase contrast imaging method. In this study we present evidence related to the presence of Si in a Si-magnetite lattice in the form of a discrete nano-phase, or nano-precipitates within the host magnetite derived from Z-contrast imaging methodology. The Z-contrast imaging can clearly reveal positions of atom and vacancy columns along electron beam direction. Crystal structures of nano-phases in a fayalite – laihunite (or α-$Fe_{1.5}SiO_4$) series have been solved by combining Z-contrast imaging and density functional theory (DFT) method (Xu et. al, 2014).

Samples and Experimental Method

The samples in this study come from drill hole (DDH)-47A located ~15 km south of Wittenoom, Western Australia (Zone 50 627013E 7529757N). Rock removed from DDH-47A was used to define the stratigraphic subdivisions of the Brockman Iron Formation, Hamersley Group, Mt. Bruce Supergroup and is the type section core for the Dales Gorge Member (Trendall and Blockley, 1968). Our samples are taken from quarter-core sections of DDH-47A selected by Cornelius Klein in 1978. Klein donated these samples to the Department of Geoscience, UW-Madison, and they are catalogued in the collections of the UW-Madison Geology Museum (UWGM500). Details regarding the samples have been described previously (Huberty et al., 2012).

Scanning transmission electron microscopy (STEM) analyses were carried out using a FEI Titan 80-200 aberration corrected scanning/transmission electron microscope operated at 200 kV. The microscope is equipped with CEOS probe aberration corrector, an EDAX high resolution EDS detector, and Gatan image filtering system. Probe current was set at 24.5 pA. All the Z-contrast images were acquired using camera length of 160 mm, in order to maximize the difference among different elements. High-angle annular dark-field (HAADF) STEM imaging (or Z-contrast imaging) is capable of a spatial resolution of <0.1 nm using the aberration-corrected STEM. Signal intensity is proportional to a power function of atomic number ($\sim Z^{2.27}$) and the number of atoms along the beam direction for the imaging acquisition condition (Shi, 2014; Xu et al., 2014). Samples of silician magnetite (~ 2 wt% of Silica) were selected for this Z-contrast imaging study. TEM samples were prepared by crushing selected silician magnetite fragments between two glass slides with ethanol. A drop of the suspension was placed on a

lacey-carbon coated Cu grid and air dried. The STEM sample was lightly plasma cleaned before it was inserted into the TEM column. All images presented here are of acquired raw data without further image processing.

Density functional theory (DFT) calculations were performed using Vienna *ab initio* simulation code (VASP) (Kresse et al., 1996). The general gradient approximation (GGA) with Perdew, Burke, and Ernzerhof (PBE) parameters was employed (Perdew et al., 1996). The projector-augmented wave (PAW) method with the energy cutoff of 600 eV was also used. Monkhorst-Pack meshes of 2×2×2 k-point were found to be sufficient for magnetite and silician magnetite structures. In order to take into account the on-site Coulomb repulsion of 3d electron in Fe atoms, a simplified (rotationally invariant) approach to GGA+U (Dudarev et al., 1998) was carried out. In Dudarev's method, an effective U parameter, $U_{eff} = U-J$, is used, where, U is the effective on-site Coulomb interaction parameters, and J is the effective on-site Exchange interaction parameters. A U_{eff} value of 3.8 eV was fitted against the band gap in the low-symmetry unit cell below the Verwey temperature (Roldan et al., 2013). Since silician magnetite is a nano phase, there are no bulk properties of magnetite against which we can fit the U_{eff}. For silician magnetite, a U_{eff} value of 3.8 eV was used for GGA+U calculation of silician magnetite. The cell edge and all atoms were fully relaxed until the required accuracy was reached.

Results and Discussions

STEM results

Low magnification annular bight-field (ABF) STEM image (left) and HAADF STEM imaging (i.e., Z-contrast image) of the silician magnetite shows precipitates (indicated by yellow arrows) of Si-magnetite as depicted in Figure 1. Local domains with low intensity are obvious in thin area of the Z-contrast image (Fig. 1B). These domains have shapes of {111} and are coherent with the host magnetite. The domains have thickness of $2d_{111}$, $4d_{111}$ and $6d_{111}$. Some domains show doubled periodicity along the [111] direction. This characteristic is more obvious in thick areas of the ABF image (Fig. 1A). A fast Fourier transform (FFT) pattern from Z-contrast imaging indicates that the image has resolution of ~ 1 Å. X-ray EDS spectra from the precipitates show relatively higher Si peak intensity than those from neighboring areas without precipitates, although fluorescence from a Li-drifted silicon detector will result in a weak Si peak in EDS spectra even from Si-free area.

A high-resolution Z-contrast image from a precipitate shows bright spots corresponding to positions of atom columns along the beam direction (Fig. 2B). Plots of magnetite along the [110] zone axis have also been overlaid on the ABF and Z-contrast images. Green dots represent Fe^{3+} in tetrahedral sites. Orange dots represent Fe^{2+} and Fe^{3+}(III) in octahedral sites. Different sizes of the orange dots indicate that the number of Fe atoms along the beam direction is doubled for the bright spots as compared to less bright spots.

In Z-contrast image, intensity is proportional to atomic number (Z) and the number of atoms (m) along the beam direction ($I \sim mZ^n$). The contrast in the ABF image is roughly reversed (Fig. 2A). The ABF image also shows positions oxygen (upper-right corner of Fig. 2A). The Z-contrast image (right) shows local positions of atoms over a large range of thicknesses, whereas

the ABF image (left) shows contrast change from thin (top) to thick (bottom) areas due to its phase contrast. Intensity of the Z-contrast image increases monotonically with thickness because Z-contrast images are incoherent images obtained with a high-angle annular detector (Kirkland, 1998; Pennycook, 2002).

One precipitate has width of $4d_{111}$. An intensity profile along the dashed line shows that intensity drops for the atom columns in the precipitate (Fig. 2C). Intensity from an atom column for the experiment condition is related by $I \sim m Z^n$, where, m is the numbers of atoms along the beam direction (related to thickness and occupancies), and n is about 2 (n=2.27 for the experiment condition) (Shi, 2014). If thickness is the same, the intensity is related to occupancies of atoms in the column site. For instance, intensity from tetrahedral Fe sites in the host magnetite is expressed by $I \sim Z^n_{Fe}$. The intensity from the tetrahedral (T) site in the precipitate area is expressed by $I \sim (1-x) Z^n_{Fe} + x Z^n_{Si}$, where x is fraction of Si-magnetite in the column site. The intensity from octahedral Fe sites is $I \sim 2(1-y) Z^n_{Fe}$ and $I \sim (1-y) Z^n_{Fe}$ for the two types of Fe column sites, where y is the fraction of vacancies in the octahedral Fe sites. The intensity reduction for the tetrahedral sites (T sites) is due to the presence of Si in the Si-magnetite precipitate. The intensity drop in the octahedral columns (labeled with 2Fe-) is due to vacancies which exist in order to maintain the charge balance disturbed by Si^{4+} in the neighboring tetrahedral sites. Overlap of the precipitate and host magnetite occurs in these locations.

Z-contrast imagery from another Si-magnetite precipitate with width of $4d_{111}$ shows the largest intensity difference across the precipitate and also exhibits similar features compared to the previous example (Fig. 3). The precipitate has less overlap with the host magnetite in this area.

Intensity profiles along the dashed lines (line-c and line-d) show intensity reduction in the precipitate with respect to the host magnetite (Fig. 3C, 3D). In this case Si replaces Fe^{3+} in tetrahedral sites and vacancies are introduced in octahedral sites.

Although both the host and precipitate have same structure, Z-contrast images show intensity drop in the precipitates (Fig. 2-4). Intensity profiles along the dashed b- and c- lines show intensity reduction in the octahedral columns (labeled by 2Fe-, and Fe-) with respect to columns without vacancies (labeled by 2Fe, Fe) in the host magnetite (Fig. 4). Again in this case, Si replaces Fe^{3+} in tetrahedral sites, and vacancies are introduced in octahedral sites.

The evidence presented here supports Si substitution into tetrahedral coordination in silician magnetite as has been suggested by others (Newberry et al., 1982, Westendorp, 1991; Shimazaki, 1998; Ohkawa et al., 2007).

One proposed mechanism used to explain this phenomenon is a fayalite component replacing magnetite (Newberry et al., 1982).

$$Fe_3O_4 \leftrightarrow Fe_2SiO_4, \text{ or} \quad (1a)$$

$$[Fe^{3+}]^{IV} + [Fe^{3+}]^{VI} \leftrightarrow [Si^{4+}]^{IV} + [Fe^{2+}]^{VI} \quad (1b)$$

If a fayalite component were to replace magnetite, the intensity reduction would only occur in tetrahedral sites, not in octahedral sites. Obviously, this mechanism does not fit the observed intensity drops from octahedral Fe sites in the obtained Z-contrasts images (see profiles in Figs. 2-4) and electron microprobe analysis (EMPA) data (see trend line 1 in figure 5). It has also been suggested that Si is present in tetrahedral coordination in magnetite. This hypothesis calls upon

177 octahedral vacancies to account for the difference between previously observed EPMA data and
178 coupled ferrous iron substitution (Ohkawa et al., 2007). This replacement may be expressed as

179 $3[Fe^{3+}]^{IV} + [Fe^{3+}]^{VI} \leftrightarrow 3[Si^{4+}]^{IV} + \square^{VI}$, or (2a)

180 $2Fe^{3+} + (2/3)[Fe^{3+}]^{VI} \leftrightarrow 2[Si^{4+}]^{IV} + (2/3)\square^{VI}$, or (2b)

181 $[Fe^{3+}]^{VI}[Fe^{2+}]^{VI}[Fe^{3+}]^{IV}O_4 \leftrightarrow [\square_{0.33}Fe^{3+}_{0.67}Fe^{2+}]^{VI}Si^{IV}O_4$, or (2c)

182 where the symbol "□" means vacancy.

183 However, this mechanism does not fit the newly observed EPMA data from magnetite in this
184 study (see trend line 2 in Figure 5). Extra vacancies are required in order to reconcile the trend of
185 the experimental EPMA data.

186

187 Z-contrast images clearly show lower intensity from the octahedral sites in the Si-Fe-domains
188 with respect to the host magnetite (see intensity profiles in Figs. 2-4). When Si replaces Fe^{3+} in
189 tetrahedral sites it will introduce vacancies in octahedral sites. The vacancies can be generated by
190 removing Fe^{3+} or Fe^{2+} in octahedral sites. If vacancies result from removing Fe^{3+} in octahedral
191 sites, one Si substitution will result in 1/3 vacancies. The trend line will exhibit a higher slope
192 (than that for the observed data points) (i.e., trend line 2 in Fig. 5). This mechanism can be
193 expressed as exchange mechanism (2). If vacancies result from removing Fe^{2+} in octahedral
194 sites, one Si will result in 1/2 vacancies. This exchange mechanism may be expressed as

195 $[Fe^{3+}]^{VI}[Fe^{2+}]^{VI}[Fe^{3+}]^{IV}O_4 \leftrightarrow [\square_{0.5}Fe^{3+}Fe^{2+}_{0.5}]^{VI}Si^{IV}O_4$, or (3a)

196 $2[Fe^{3+}]^{IV} + [Fe^{3+}]^{VI} \leftrightarrow 2[Si^{4+}]^{IV} + \square^{VI}$. (3b)

The trend line based on this mechanism matches the observed data points very well (i.e., trend line 3 in Fig. 5). The ideal relationship between Si apfu and total cations, Σ (Fe + Mg, Zn, Al, Ti, Mn) or, ΣM apfu based on exchange (3a) is Si = - (2/3) (ΣM) + 2. This is very close to a linear relation fit of the data (Huberty et al., 2012): Si = - 0.6771 (ΣM) + 2.0304. Mathematically, the proposed exchange mechanism (3) can be considered as linear combination mechanism (2b) and maghemite replacement (4):

$$[Fe^{3+}]^{VI}[Fe^{2+}]^{VI}\,[Fe^{3+}]^{IV}O_4 \leftrightarrow [\square]^{VI}_{0.333}[Fe^{3+}]^{VI}_{0.667}[Fe^{3+}]^{IV}_2O_4, \text{ or} \qquad (4a)$$

$$[Fe^{3+}]^{IV} + [Fe^{3+}]^{VI} + [Fe^{2+}]^{VI} \leftrightarrow 2[Fe^{3+}]^{IV} + (2/3)[Fe^{3+}] + (1/3)\square^{VI}. \qquad (4b)$$

The Si-magnetite nano-precipitates overlap with the host magnetite. Intensities from the precipitate areas are form both the Si-magnetite ($[\square_{0.5}Fe^{3+}\ Fe^{2+}_{0.5}]^{VI}Si^{IV}O_4$) and the host magnetite below or above the precipitate. The profiles from the Z-contrast images explain the relationship between Si replacing the tetrahedral Fe and vacancies introduced in the octahedral Fe^{2+} sites. Based on the measured intensities, the average ratio between the vacancy (y) and Si in tetrahedral sites (x) is about ½. Both EMPA data and Z-contrast imagery support this exchange mechanism (3) (Fig. 5). The substitution or exchange requires both charge balance and size-match between tetrahedra and octahedra in the structure. Replacing Fe^{3+} in tetrahedral sites by Si will reduce the size of tetrahedra. In order for Si-magnetite structure to accommodate the Si-O_4 tetrahedra, size of the octahedra needs to be reduced too. Keeping Fe^{3+} and producing more vacancies in the octahedral sites will fit the Si-magnetite structure better than keeping Fe^{2+} and producing less vacancies in the octahedral sites.

The observed trend line is resulted from areas with different amounts of γ-$Fe_{1.5}SiO_4$ nano-precipitates in the analyzed magnetite. Si is in discrete nano-phases of γ–$Fe_{1.5}SiO_4$, instead of homogenously distributed in the magnetite crystal. The precipitates have the same stoichiometry as laihunite-1M (α-$Fe_{1.5}SiO_4$) according to a proposal by Fu et al. (1982) and Xu et al., (2014). Oxygen atoms in laihunite follow hexagonal closest packing (Fu et al., 1982). Oxygen atoms in the Si-magnetite precipitates follow cubic closest packing. The presence of γ–$Fe_{1.5}SiO_4$ precipitates indicates that the γ-$Fe_{1.5}SiO_4$ nano-phase could be more stable than a precipitate of silica polymorph within the host magnetite at low temperature.

Some areas of the magnetite show periodic intergrowth of Si-magnetite (111) layers with thickness of $2d_{111}$ and magnetite (111) layers with thickness of $1d_{111}$ (Fig. 6). We propose that occurrence of the thin (111) layers of the Si-magnetite within the magnetite host will dissipate or reduce interfacial energy between the precipitates and the host due to small differences in unit cell edges between the precipitate and the host magnetite. This is very similar to Guinier-Preston zones (G.P. zones) in orthopyroxene (Nord, 1980) and mixed-layer clay minerals such as interstratified chlorite/serpentine (Banfield and Bailey, 1996; Xu and Veblen, 1996). A structure diagram for the interstratified Si-magnetite / magnetite is schematically illustrated in Figure 7.

Structure of γ-$Fe_{1.5}SiO_4$ with ordered vacancies

We have performed DFT calculations for magnetite and Si-magnetite. The calculated *a*-dimension unit cell edge for magnetite is 8.402 Å, which is in good agreement with experimental data (Fleet, 1981; Wechsler et al., 1984). The same calculation parameters were used for

241 calculating the Si-magnetite structure with ordered vacancies. The proposed replacement
242 mechanism indicates that Si^{4+} and vacancies are in the tetrahedral Fe^{3+} and octahedral Fe^{2+} ion
243 sites, respectively. At low temperature, ordering of the vacancies may occur in the structure. The
244 initial structures were constructed using the magnetite lattice parameters and removing four Fe^{2+}
245 from the 16 octahedral iron atoms in one unit cell (leaving 8 Si atoms, 12 Fe atoms and 32 O
246 atoms within one unit cell). There are two possible configurations of vacancies for ordered γ–
247 $Fe_{1.5}SiO_4$. The results show that vacancies in the low energy configuration are very similar to
248 those in a cubic maghemite structure as reported by Shmakov et al. (1995). The unit cell edge
249 length at 0K is 8.125 Å. Calculated results indicate that the ordered γ–$Fe_{1.5}SiO_4$ is more stable
250 than α-$Fe_{1.5}SiO_4$ (laihunite) by at 0K, although both nano-precipitates occur in their host
251 minerals of magnetite and fayalite. Vacancy disordering at high temperature may increase the
252 unit cell edge slightly. The host magnetite may also confine the unit cell edge of the Si-magnetite
253 precipitates due to the coherent boundary between the host magnetite and the precipitate.
254 Fractional coordinates for the atoms in Si-magnetite are listed in Table 1. The fractional
255 coordinates provided in Table 1 represent DFT calculation data and that they are not resulting
256 from refinement procedures applied to experimental data sets. Consequently, uncertainties are
257 not provided for the numbers given in the table. Structural models for the Si-magnetite with
258 disordered and ordered vacancies are illustrated in Fig. 8.

259

260 **Implications**

261 The amount of Si in magnetite may be related to temperature, pressure, and even oxygen
262 fugacity (Newberry et al., 1982).

Oxygen fugacity may also affect the replacement reactions:

$Fe_3O_4 \leftrightarrow Fe_{1.5}SiO_4$, or (5a)

$[Fe^{3+}]^{VI}[Fe^{2+}]^{VI}\,[Fe^{3+}]^{IV}O_4 \quad \leftrightarrow \quad [\square_{0.5}Fe^{3+}\,Fe^{2+}{}_{0.5}]^{VI}Si^{IV}O_4$ (3a)

Si-magnetite may be represented as a fictive reaction of

$Fe_3O_4 + 2SiO_2 = 2(\square_{0.5}Fe^{3+}\,Fe^{2+}{}_{0.5})^{VI}Si^{IV}O_4$. (6)

Activity of aqueous silica and Fe-silicate complexes will also affect the amount of Si in magnetite. Magnetite crystals in mafic and ultramafic rocks are generally low in silicon (Newberry et al., 1982). Silician magnetite zones may indicate relatively high temperature and activities of aqueous silica and aqueous Fe-silicate complex during crystallization as compared to other magnetite in the studied BIF sample. Aqueous Fe-silicate complex is quite stable (Wang et al., 2009). Adsorbed aqueous silica and Fe-silicate complex could be incorporated into structure of a growing magnetite and form silician magnetite. Silician magnetite may be stable under more reducing conditions than for pure magnetite. Silician magnetite will also inhibit its oxidative transformation into hematite. Synthetic lab experiments by Lund and Dumesic (1981) found that the phase transformation of magnetite to hematite in air was inhibited for silician magnetite and instead resulted in the formation of maghemite at temperatures up to 550 °C. The presence of hematite sub-micro-laminae with silician magnetite overgrowths in some banded iron formations may be resulted from selective oxidation of magnetite (Huberty et al., 2012). DFT calculation shows that Si-magnetite has an ordered distribution of vacancies. This type of material may have unique magnetic and semiconducting properties. The Si-magnetite could be ferromagnetic, because there is no Fe in the tetrahedral sites, and all the Fe in octahedral site have same spin direction. The methods used in this study can be applied to enhance the understanding of other

285 crystal structures, nano-phases, and nano-precipitates that are minor components in a variety of
286 host minerals (Xu et al., 2014).

287

288 **ACKNOWLDEGEMENTS**

289 This work is supported by NASA Astrobiology Institute (N07-5489). Authors thank Dr. Alex Kivit for
290 helping in STEM analyses, and two anoumynous reviewers for helpful comments and suggestions.
291 Author also thank Major Research Instrumentation (MRI) Program of NSF for funding the aberration-
292 corretced STEM.

293

References

Banfield, JF, and Bailey, SW (1996) Formation of regularly interstratified serpentine – chlorite minerals by tetrahedral inversion in long-period serpentine polytypes. American Mineralogist, 81, 79-81.

Dudarev, SL, Botton, GA, Savrasov, SY, Humphreys, CJ and Sutton, AP (1998) Electron-energy-loss spectra and the structural stability of nickel oxide: An LSDA+U study. Physical Review B, 57, 1505-1509.

Fleet, M. E. (1981) The structure of magnetite. Acta Crystallographica, B37, 917-920.

Fu, P Kong, Y and Zhang, L (1982) Domain twinning of laihunite and refinement of its crystal structure. Chinese Journal of Geochemistry 1: 115-133.

Huberty, J. M., Konish, H., Heck, P. R., Fournelle, J. H., Valley, J. W., and Xu, H. (2012) Silician magnetite from the Dales Gorge member of the Brockman iron formation, Hamersley Group, western Australia. American Mineralogist, 97, 26-37.

Imai, A. (2001) Generation and Evolution of Ore Fluids for Porphyry Cu-Au Mineralization of the Santo Tomas II (Philex) Deposit, Philippines. Resource Geology, 51, 2, 71-76.

Kirkland, E.J. (1998) Advanced computing in electron microscopy. Plenum Press, New York, 250 pp.

Kresse, G, and Furthmüller, J (1996) Efficiency of ab-initio total energy calculations for metals and semiconductors using a plane-wave basis set. Computational Materials Science, 1, 15-50.

Lund, C.R.F. and Dumesic, J.A. (1981) Strong oxide-oxide interactions in silica-supported magnetite catalysts. 1. X-ray diffraction and Mössbauer spectroscopy evidence for interaction. Journal of Physical Chemistry, 85, 3175-3180.

Newberry, N.G., Peacor, D.R., Essene, E.J. and Geissman, J.W. (1982) Silicon in Magnetite: High-Resolution Microanalysis of Magnetite-Ilmenite Intergrowths. Contributions to Mineralogy and Petrology, 80, 334-340.

Ohkawa, M., Miyahara, M., Ohta, E. and Hoshino, K. (2007) Silicon-substituted magnetite and accompanying iron oxides and hydroxides from the Kumano mine, Yamaguchi Prefecture, Japan: Reexamination of the so-called maghemite (γ-Fe_2O_3). Journal of Mineralogical and Petrological Sciences, 102, 182-193.

Roldan, A., Santos-Carballal, D., and de Leeuw, N.H. (2013) A comparative DFT study of the mechanical and electronic properties of greigite Fe_3S_4 and magnetite Fe_3O_4. Journal of Chemical Physics, 138, 204712.

Pennycook, S (2002) Structure determination through Z-contrast microscopy. Advances in imaging and electron physics, 123, 173-206.

Perdew, J.P., Burke, K and Ernzerhof, M (1996) Generalized gradient approximation made simple. Physical Review Letters, 18, 3865-3868.

Shi, F. (2013) Advanced electron microscopy of novel ferromagnetic materials and ferromagnet / oxide interfaces in magnetic tunnel junctions. Ph. D. Dissertation, University of Wisconsin - Madison.

Shiga, Y. (1988) Silician Magnetite from the Kamaishi Mine, Japan. Mining Geology, 38, 5, 437-440.

Shiga, Y. (1989) Further Study on Silician Magnetite. Mining Geology, 39, 5, 305-309.

Shmakov, A., Kryukova, G., Tsybulya, S., Chuvilin, A., and Solovyeva, L. (1995) Vacancy ordering in γ-Fe_2O_3: Synchrotron X-ray powder diffraction and high-resolution electron microscopy studies. Journal of Applied Crystallography, 28,141-145.

Shimazaki, H. (1998) On the Occurrence of Silician Magnetites. Resource Geology, 48, 1, 23-29.

Nord, G. L. (1980) The composition, structure, and stability of Guinier-Preston zones in lunar and terrestrial orthopyroxene. Physics and Chemistry of Minerals, 6: 109 – 128.

Wang, L.J., Shimazaki, H., and Shiga, Y. (2001) Skarns and Genesis of the Huanggang Fe-Sn Deposit, Inner Mongolia, China. Resource Geology, 51, 4, 359-376.

Wang, Y. Xu, H., Merino, E. and Konishi, H. (2009) Generation of banded iron formations by internal dynamics and leacing of oceanic crust. Nature Geoscience, 2, 781-784.

Wechsler, B.A., Lindsley, D.H., and Prewitt, C.T. (1984) Crystal structure and cation distribution in titanomagnetites (Fe_3-xTi_xO_4). American Mineralogist, 69, 754-770

Westendorp, R.W. and Watkinson, D.H. (1991) Silicon-bearing zoned magnetite crystals and the evolution of hydrothermal fluids at the Ansil Cu-Zn mine, Rouyn-Noranda, Quebec. Economic Geology, 86, 1110-1114.

Whitney, J.A., and Stormer, J.C. Jr, (1976) Geothermometry and geobarometry in epizonal granitic intrusions: A comparison of iron-titanium oxides and coexisting feldspars. American Mineralogist, 61, 751-763.

Xu, H., and Veblen, D.R. (1996) Interstratification and other reaction microstructures in the chlorite-berthierine series. Contribution to Mineralogy and Petrology, 124, 291-301.

Xu, H., Shen, Z, Konishi, H., Fu, P., and Szlufarska, I. (2014) Crystal structures of laihunite and intermediate phases between laihunite-1M and fayalite: Z-contrast imaging and *ab initio* study. American Mineralogist (in press).

Figures captions

Figure 1: Low magnification annular bight-field (ABF) STEM image (A) and HAADF STEM image (Z-contrast image) (B) of the silician magnetite. Local domains with low intensity (arrowed areas in B) are obvious in Z-contrast image, especially in thin areas (upper part of the image).

Figure 2: High-resolution ABF STEM image (A) and Z-contrast image (B) showing one nano-precipitate phase within the host magnetite. Bright spots in the Z-contrast image correspond to positions of atom columns. The number of Fe atoms along the beam direction is doubled for the bright spots with respect to less bright spots. A structure model of magnetite is overlaid on the images. Green spots correspond to Fe(III) in tetrahedral sites. Orange dots correspond to Fe(II) and Fe(III) in octahedral sites. Different sizes of orange dots indicate the number of Fe atoms along the beam direction. The Fe atoms at the large orange spot positions are doubled with respect to smaller orange and green spot positions.

Figure 3: A Z-contrast image showing the largest intensity difference across the precipitate. The precipitate has less overlap with the host magnetite in this area.

Figure 4: Z-contrast image showing a thin nano-precipitate with thickness of $2d_{111}$. The precipitates are of the Si-magnetite phase, although both the host and precipitates have the same

374 structure. Intensity line profiles can indicate occupancies of Si in tetrahedral sites (T) and
375 vacancies in octahedral sites (labeled by 2Fe-, and Fe-).

376

377 Figure 5: Plot of EMPA data and three proposed mechanism (trends). Only the mechanism of γ-
378 $Fe_{1.5}SiO_4$ nano-precipitates in the host magnetite (trend line 3) fits the data well. EPMA data
379 points are from Huberty et al. (2012). EPMA data are plotted as total cations, Σ (Fe + Mg, Zn,
380 Al, Ti, Mn) apfu on the x-axis against Si apfu on the y-axis. The denoted exchange (trend line 3)
381 is in fact identical to what is called exchange mechanism (3) in the text.

382

383 Figure 6: Z-contrast image illustrating periodic stacking of (111) layers of Si-magnetite and
384 magnetite (B). FFT pattern from the area shows tripled periodicity (arrowed) along the [111]
385 direction (A). Intensity profile (C) also shows relatively lower intensity from the Si-magnetite
386 (111) layers with respect to the neighboring magnetite layers.

387

388 Figure 7: A structural diagram schematically illustrates interstratified Si-magnetite / magnetite
389 along the [111] direction. The interstratified structure will have lower symmetry instead of cubic
390 symmetry. Blue dots represent Si atoms.

391

392 Fig. 8: Structure models for the disordered Si-magnetite with *Fd3m* symmetry (A, C) and the
393 ordered Si-magnetite with $P4_332$ symmetry (B, D). The unit cell edge length for the disordered
394 Si-magnetite will be slightly longer than that of the ordered one.

Fig. 1

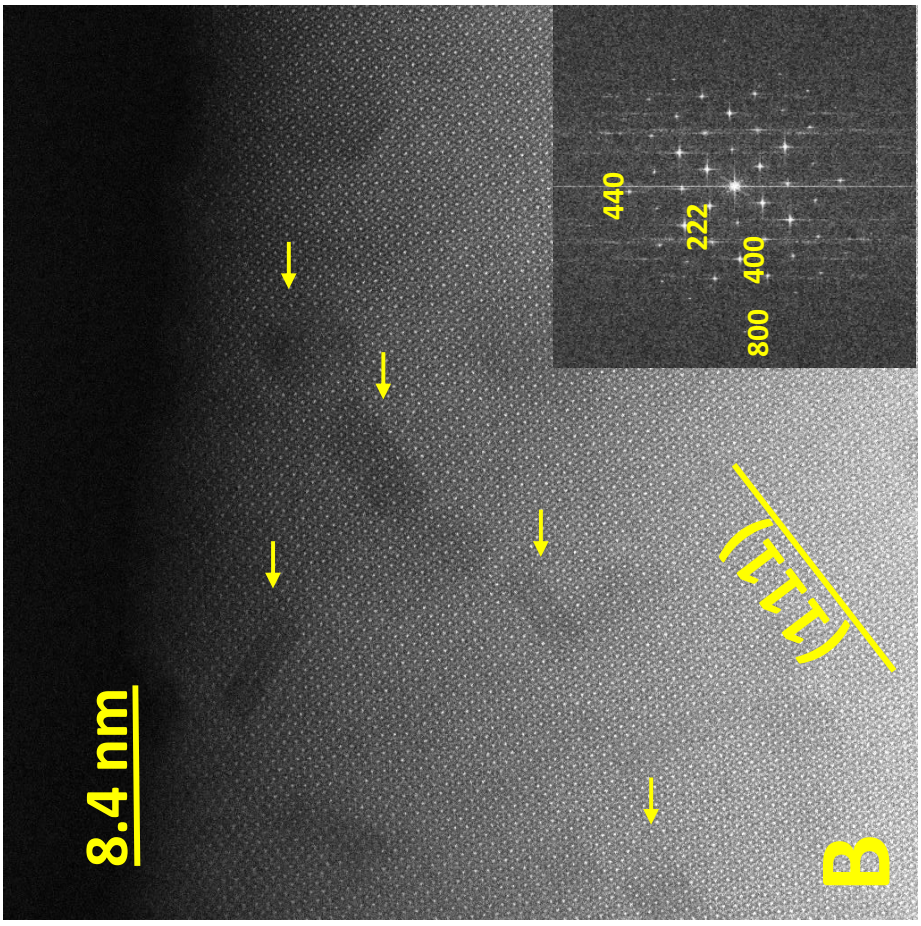

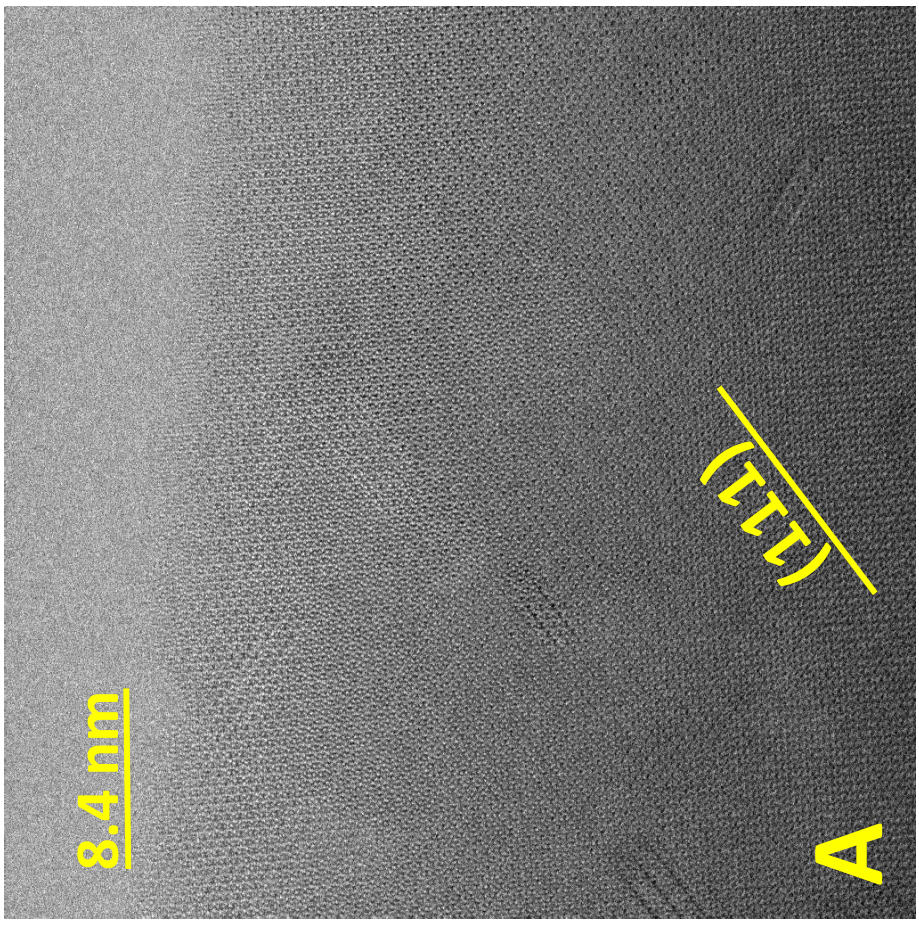

Fig. 2

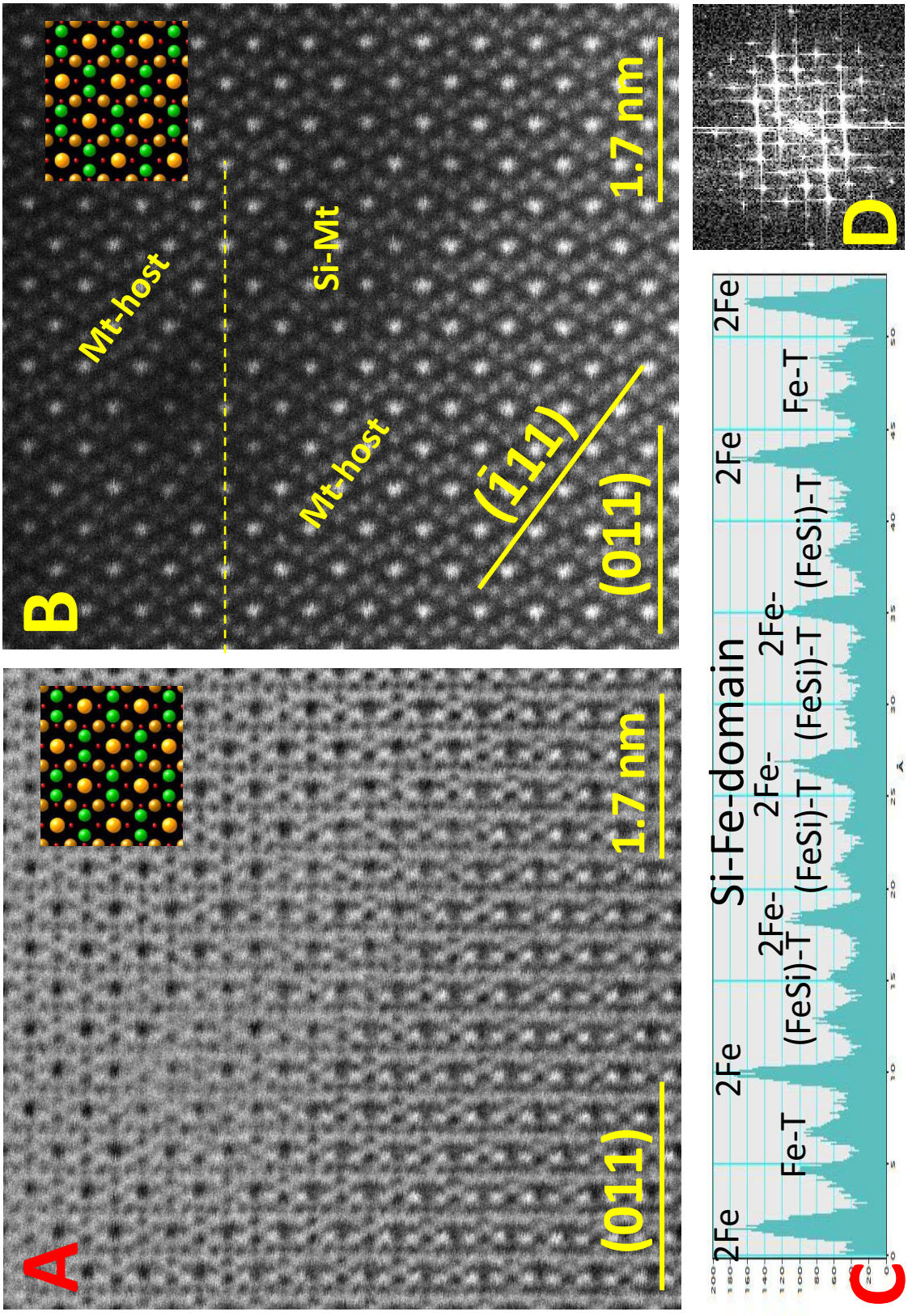
A
(011)
1.7 nm
B
Mt-host
Si-Mt
Mt-host
(i11)
(011)
1.7 nm
D
C
Si-Fe-domain
2Fe
2Fe
2Fe
2Fe
Fe-T
Fe-T
2Fe-
(FeSi)-T
2Fe-
(FeSi)-T
2Fe-
(FeSi)-T
Å

This is a preprint, the final version is subject to change, of the American Mineralogist (MSA)
Cite as Authors (Year) Title. American Mineralogist, in press.
(DOI will not work until issue is live.) DOI: http://dx.doi.org/10.2138/am-2014-4964

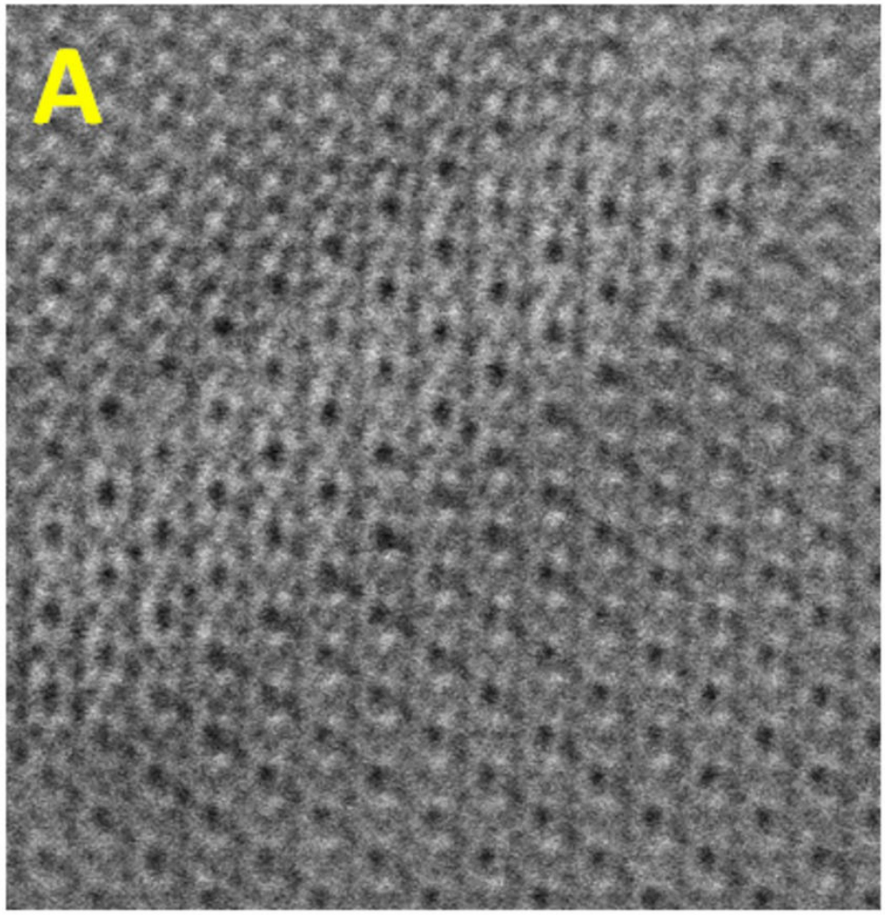

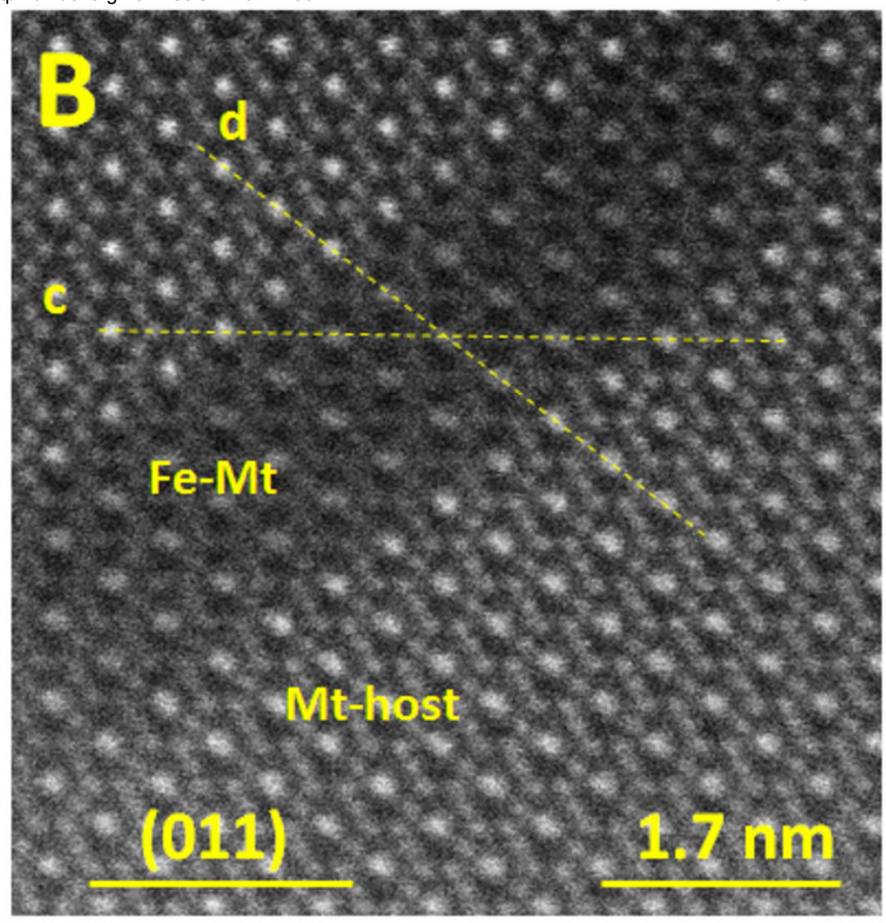

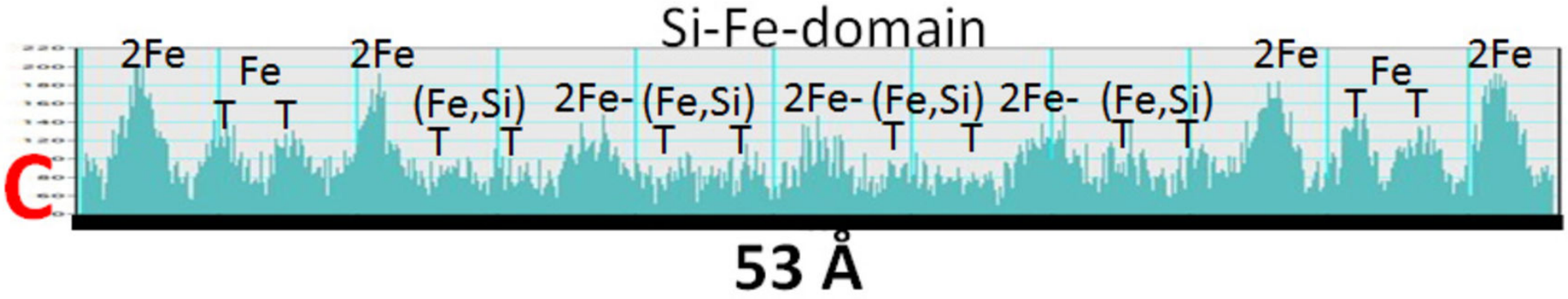

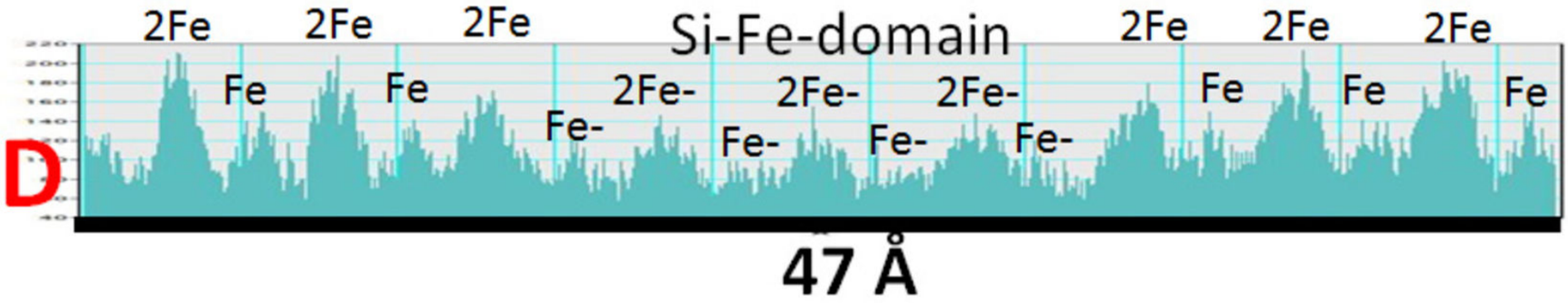

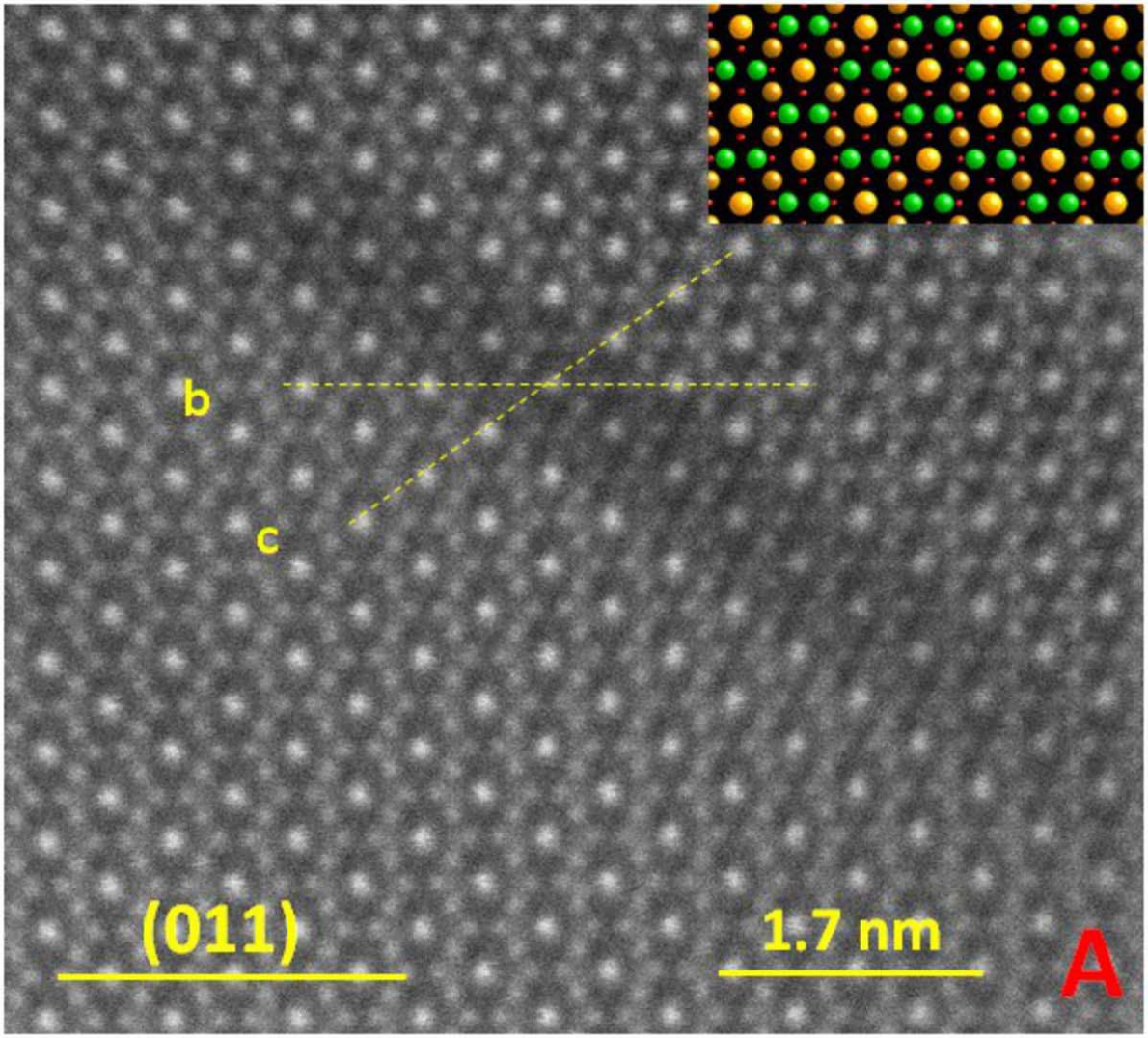
b
c
(011)
1.7 nm
A

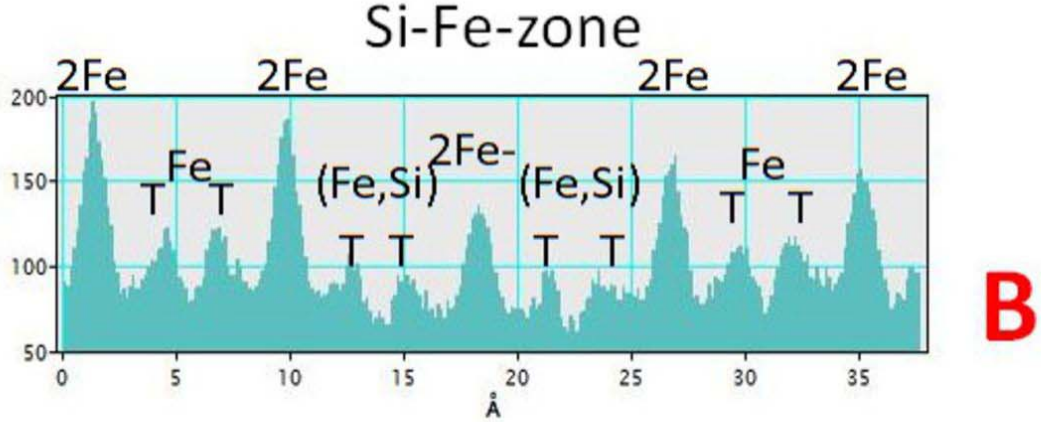
Si-Fe-zone
2Fe
2Fe
2Fe
2Fe
Fe
T
T
(Fe,Si)
2Fe-
(Fe,Si)
T
T
T
T
T
T
Fe
T
T
200
150
100
50
0
5
10
15
20
25
30
35
Å

B

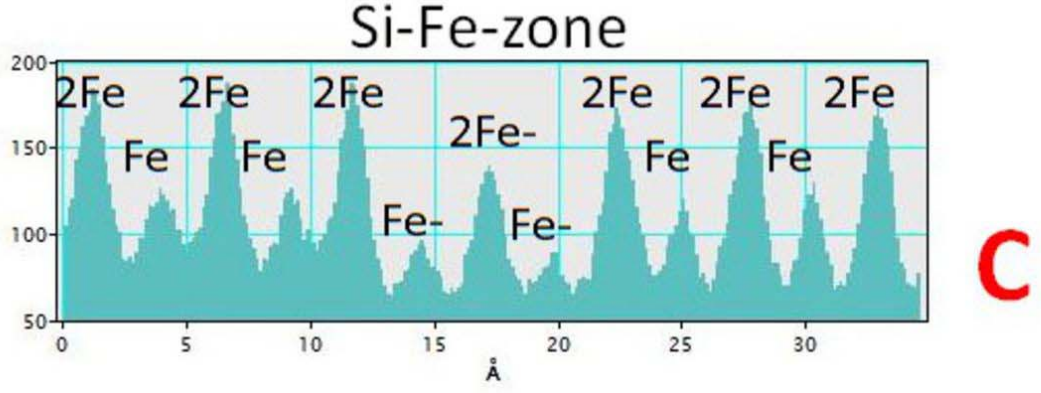
Si-Fe-zone
2Fe
2Fe
2Fe
2Fe
2Fe
2Fe
Fe
Fe
2Fe-
Fe
Fe
Fe-
Fe-
200
150
100
50
0
5
10
15
20
25
30
Å

C

Fig. 5

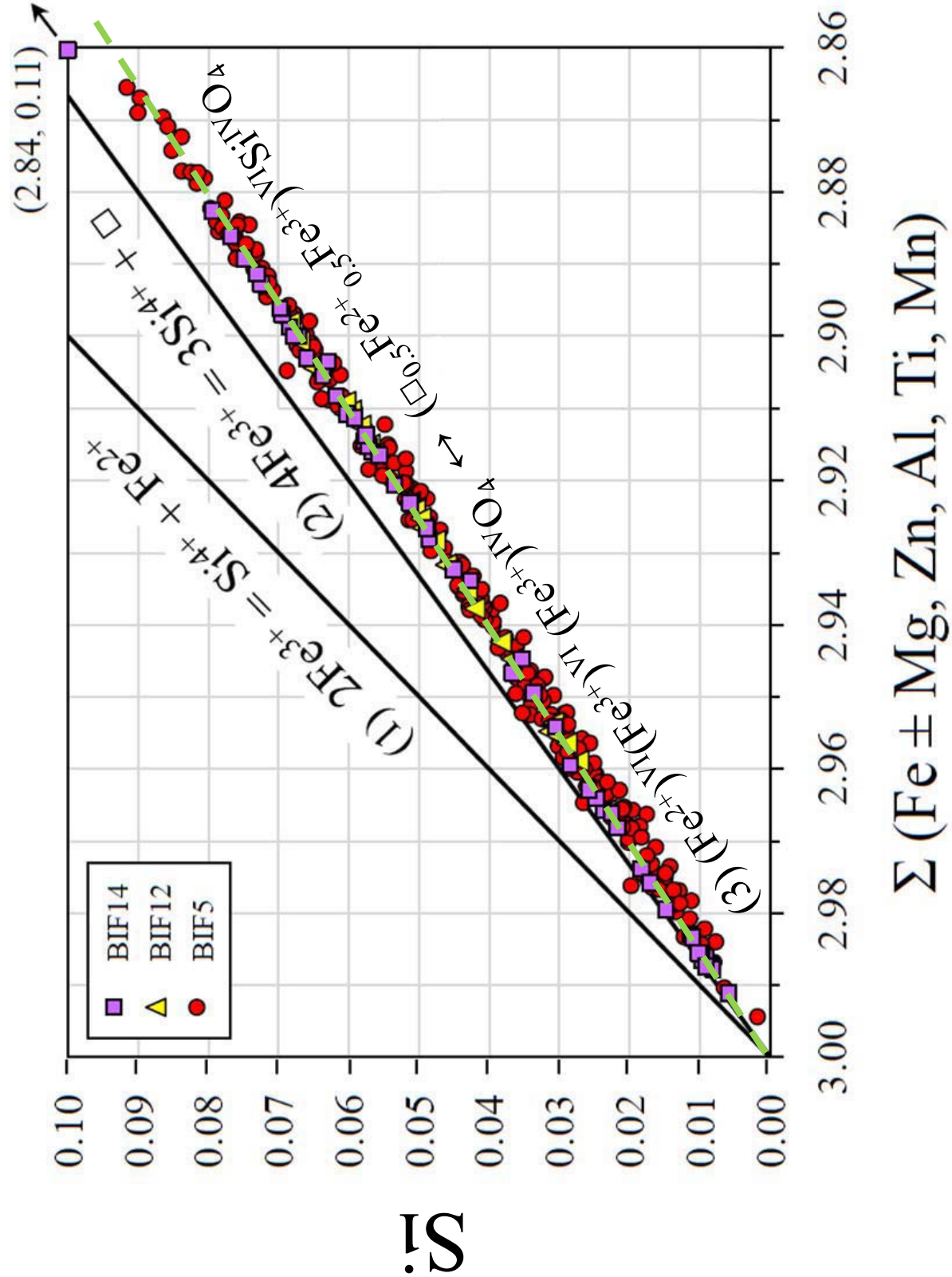
Si
Σ (Fe ± Mg, Zn, Al, Ti, Mn)
(2.84, 0.11)
BIF14
BIF12
BIF5
(1) 2Fe3+ = Si4+ + Fe2+
(2) 4Fe3+ = 3Si4+ + □
(3) (Fe2+)VI(Fe3+)VI (Fe3+)IVO4 ↔ (□0.5Fe2+ 0.5Fe3+)VISiIVO4
0.10
0.09
0.08
0.07
0.06
0.05
0.04
0.03
0.02
0.01
0.00
3.00
2.98
2.96
2.94
2.92
2.90
2.88
2.86

Fig. 6

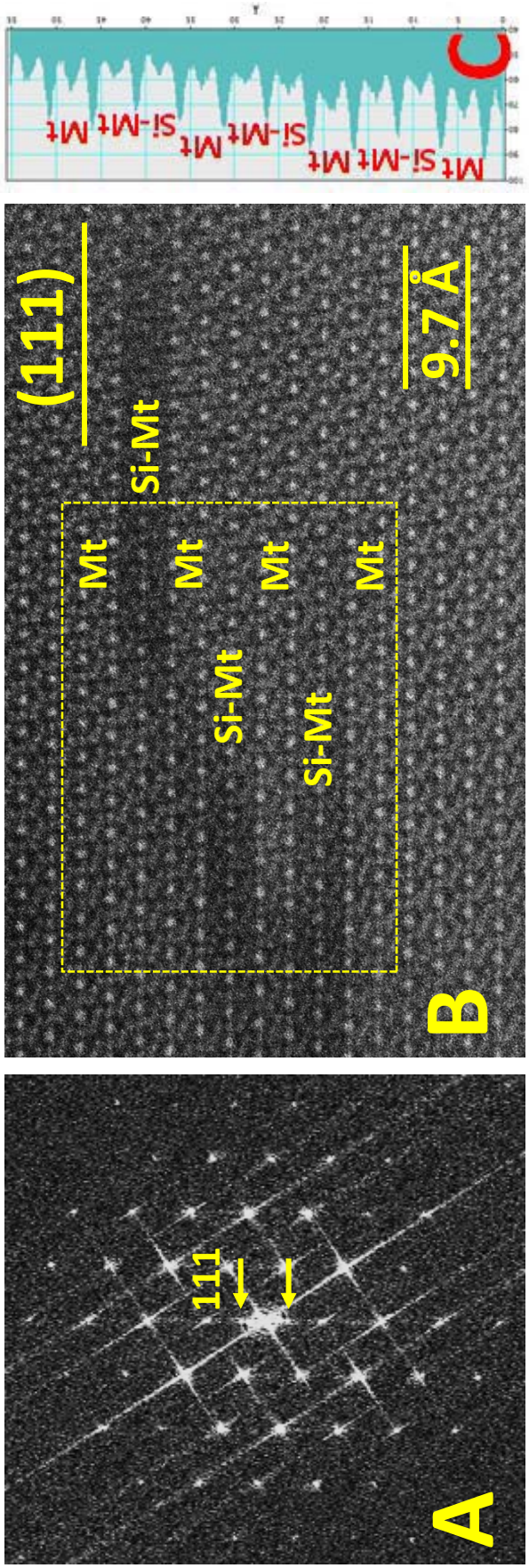
C
Mt
Si-Mt
Mt
Si-Mt
Mt
Si-Mt
Mt
(111)
Si-Mt
9.7 Å
Mt
Mt
Mt
Mt
Si-Mt
Si-Mt
B
111
A

Fig. 7

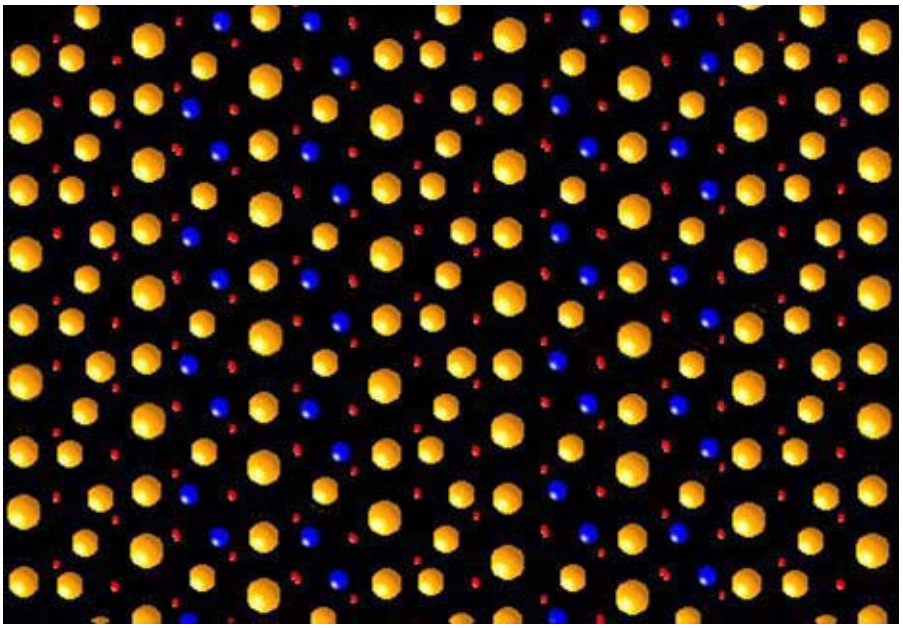

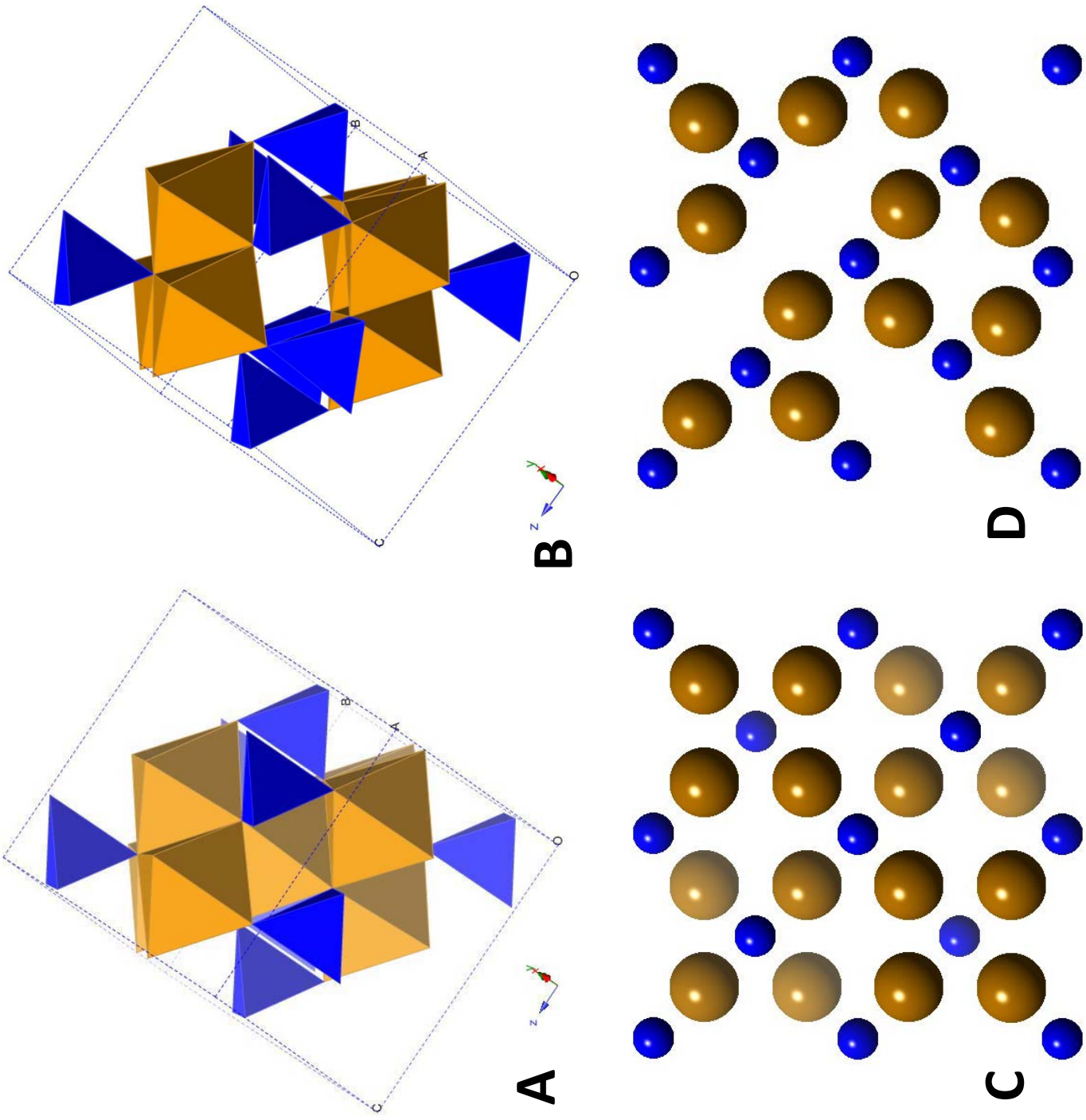

Fig. 8

Table 1: Fractional coordinates of the atoms in γ-$Fe_{1.5}SiO_4$.

Atom	**x**	**y**	**z**
Si	0.99033	0.99033	0.99033
Fe	0.85652	0.60650	0.87498
O1	0.86995	0.86995	0.86995
O2	0.37549	0.39758	0.86995

Note: Space group: $P4_332$; a = 8.12523 Å.

Cif file is available on content page of this issue.